## Supporting Information

# Hyperpolarized $^{129}$Xe atoms Sense the Presence of Drug Molecules in Nano-hosts Revealed by Magnetic Resonance Imaging

Xu Zhang[‡1, 2], Yuqi Yang[‡1,2], Yaping Yuan[1], Sen Yue[1,2], Xiuchao Zhao[1], Quer Yue[1], Qingbin Zeng[1], Qianni Guo[1], Xin Zhou[*1,2]

*[1]Key Laboratory of Magnetic Resonance in Biological Systems, State Key Laboratory of Magnetic Resonance and Atomic and Molecular Physics, National Center for Magnetic Resonance in Wuhan, Wuhan Institute of Physics and Mathematics, Innovation Academy for Precision Measurement Science and Technology, Wuhan, 430071, China. E-mail: xinzhou@wipm.ac.cn.*

*[2]University of Chinese Academy of Sciences, Beijing, 100049, China.*

*‡These authors contributed equally.*

## Table of Contents

## *Section S1* Preparation and Characterization of MOL Nano-hosts

*Materials and Instruments*

All reagents were commercially available without further purification. $HfCl_4$ (98%) were purchased from Shanghai Aladdin Bio-Chem Technology Co., LTD. 1,3,5-Tris(4-carboxyphenyl)benzene (98%, $H_3BTB$) and Formic acid (99%, HCOOH) were purchased from J&K Chemicals. N, N-dimethylformamide (DMF, AR) and ethanol (AR) were obtained from Sinopharm Chemical Reagent Co., Ltd (Shanghai, China). Indocyanine green (99%, ICG) were purchased from Bide Pharmatech Ltd.

$^1H$ NMR spectra were recorded on a Bruker NMR spectrometer at 500 MHz. Thermogravimetric analysis (TGA) was performed in air using a NETZSCH STA 449F3 and heated at a rate of 5°C per minute. The powder X-ray diffraction data were collected on a PANAlytical X'Pert Powder X-ray diffraction diffractometer with Cu Kα (λ=1.5406 Å). Zetasizer Nano-ZS particle sizer (Malvern Instruments, UK) were used for the characterization of nanosheet. Transmission electron microscopy and high-resolution transmission electron microscopy images were obtained on a JEOL JEM-2100 electron microscope. Field emission scanning electron microscope images were obtained on a Zeiss SIGMA electron microscope. Atomic force microscope data and maps were obtained on a Seiko SPA 400. All the $^{129}Xe$ NMR and MRI experiments were performed on a 400 MHz Bruker AV400 widebore spectrometer (Bruker Biospin, Ettlingen, Germany). UV-vis absorption spectra were recorded on an Evolution 220 spectrophotometer (Thermo fisher scientific). The CCK-8 absorbance was measured by an ELISA plate reader (Spectra MAX 190, Molecular Devices). Confocal fluorescence images were obtained by a laser scanning confocal microscope Nikon A1 (Nikon, Tokyo, Japan). Nitrogen adsorption measurement was performed on a MicrotracBEL Belsorp-MAX. Fluorescence imaging of mice was performed on a PerkinElmer multi-channel optical imaging system (Waltham, USA). Photoacoustic imaging of mice was obtained by using a MSOT inVision 256-TF small animal imaging system (iThera Medical GmbH, Munich, Germany).

*Synthesis procedures*

The synthetic conditions for MOL were carried out in accordance with previous studies.[1] $HfCl_4$ (14 mg, 0.0437 mmol) and $H_3BTB$ (12.5 mg, 0.0285 mmol) were dissolved in 2.05 mL of DMF with a mixture of 0.88 mL of HCOOH and 0.15 mL of distilled water. The mixture was sonicated for 10 min and then transferred to a thick-walled pressure vessel (5 mL) and kept at 120 ℃ for 2 days. The resulting white precipitate was obtained by centrifugation at 20,000 rpm for 20 min and washed three times with DMF and ethanol (v:v = 1:1). The obtained white solid was further washed with distilled water and then centrifugated. For further purification, the solids obtained in the lower layer were dialysis against distilled water for 2 days. Finally, the MOL water dispersion was stored at 4 °C.

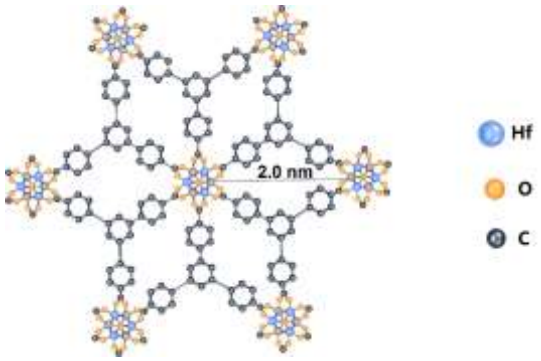


**Figure S1**. The building block of the MOL nano-hosts used in this study. MOL is connected by the basic building block ($Hf_6O_4(OH)_4(HCO_2)_6$(carboxylate)$_6$ and BTB ligands.

To further enhance water dispersibility and biocompatibility, the original MOL was fragmented into small pieces using ultrasonic treatment. First, the MOL was dispersed in distilled water at a concentration of 2 mg/mL. Then, the prepared MOL solution was subjected to ultrasonic fragmentation at a power of 260 W, with a single crushing time of 2 s and an interval of 2 s, for a total of 10 min. The entire process of ultrasonic fragment was treated in an ice bath to prevent overheating. The resulting mixture was centrifuged at 20,000 rpm for 30 min, and the resulting white solid was redispersed in distilled water and stored at 4 °C.

*Characterization of MOL*

Transmission electron microscopy (TEM) images (Figure S2a) visually displayed the wrinkled silk-like structure of MOL. Powder X-ray diffraction (Figure S2b) showed broad intralayer peaks, indicating a one-to-two-layer structure.

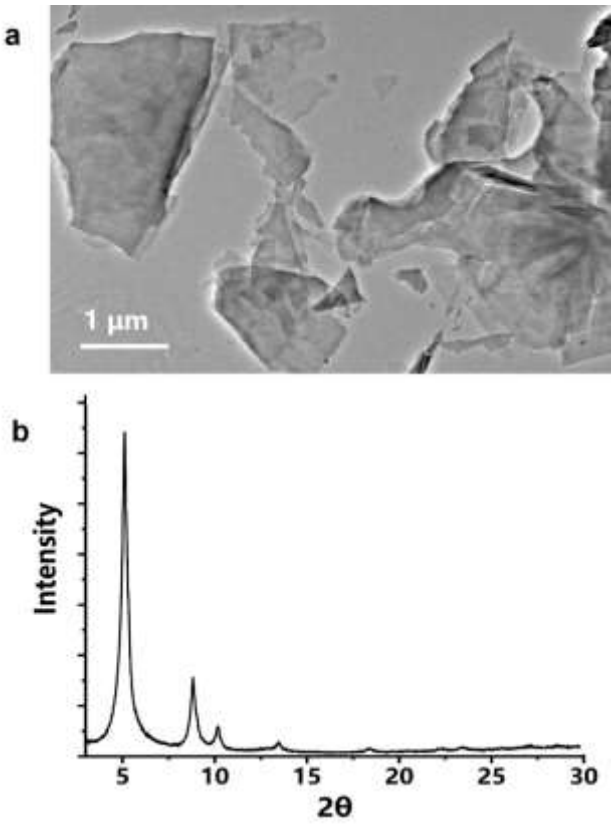


**Figure S2.** TEM image (a) and XRD (b) of the original prepared MOL.

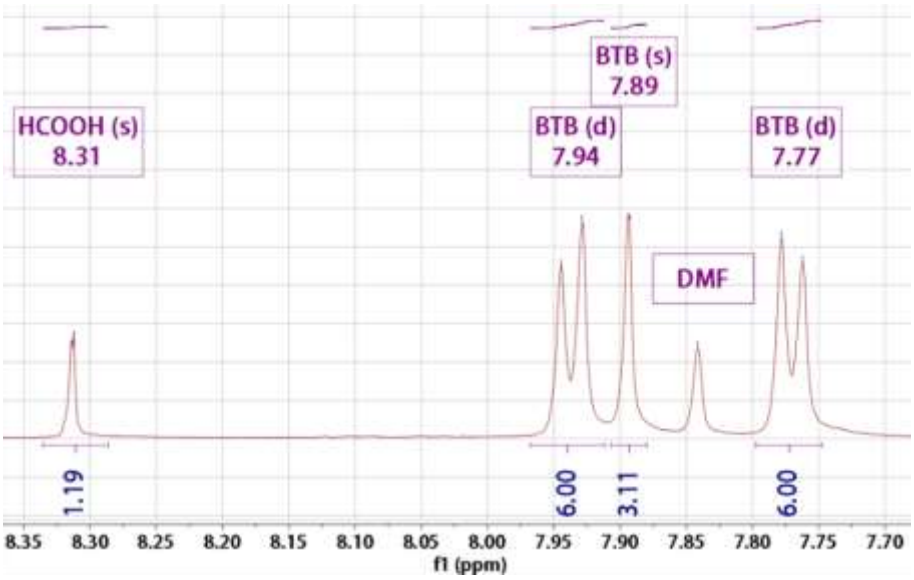


**Figure S3.** The $^{1}H$ NMR spectrum of dissolved MOL in DMSO-D6. The dried MOL was dissolved in 0.5 mL saturated $K_3PO_4$ solution of $D_2O$ and then extracted with DMSO-D6.

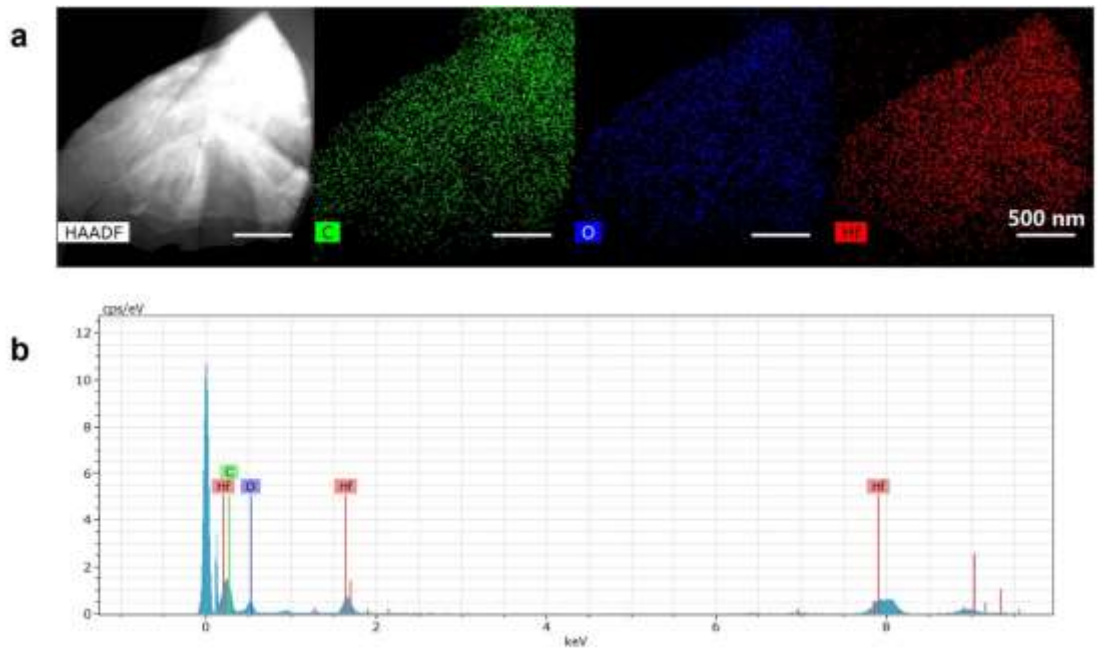


**Figure S4.** HAADF-STEM-EDX elemental mapping image (a) and EDS (b) analysis result of original prepared MOL. 63% weight and 11% atom percentage of Hafnium (aligning with the measured value of 64 wt% in the MOL determined by ICP-MS), 31% weight and 79% atom percentage of Carbon, 6% weight and 10% atom percentage of Oxygen.

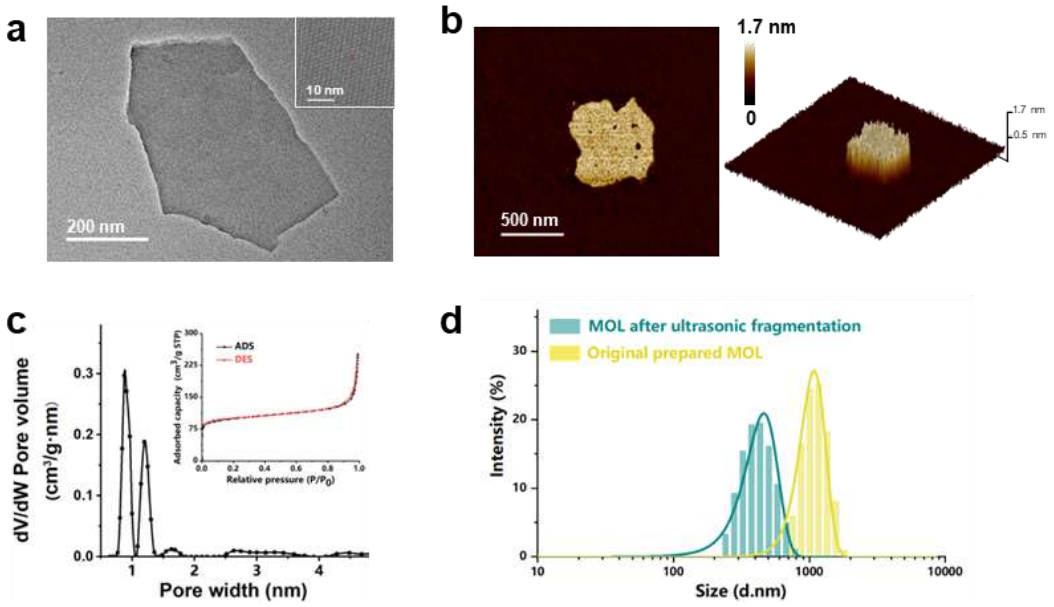


**Figure S5.** Cutting MOL into small pieces by ultrasonic fragmentation. TEM (a) and AFM (b) images indicate the thin layer structure of MOL. (c) Pore size distribution of MOL evaluated by nitrogen adsorption measurement. (d) Size distribution of MOL before and after ultrasonic fragmentation.

MOL was synthesized through a solvothermal process (Figure S1-S4) and further cut into smaller pieces (Figure S5) by ultrasonic fragmentation. High-resolution transmission electron microscopy (HRTEM) revealed clear lattice fringes measuring approximately 20.8 Å (Figure S5a); this result indicated that the microstructure of the MOL remained intact after ultrasonication. Atomic force microscope (AFM) analysis (Figure S5b) revealed an average thickness of 1.03 nm, indicating a one-to-two-layer structure. The MOL exhibited a surface area of 354.78 $m^2/g$ and a pore size distribution of 0.87 nm and 1.19 nm (Figure S5c), providing ample space for guest drug molecules and $^{129}Xe$ atoms. The average size of MOL was reduced from 1019.2 nm (yellow) to 449.6 nm (green) after ultrasonic fragmentation (Figure S5d). Furthermore, the metal content, as determined by ICP-MS, remained consistent at 64 wt% after ultrasonic fragmentation, aligning with the measured value of 63 wt% (Figure S4b) in the originally prepared MOL.

## *Section S2* NMR and MRI Measurements

*HP $^{129}$Xe CEST NMR*

Hyperpolarized $^{129}$Xe gas was produced by a home-built $^{129}$Xe hyperpolarizer. The $^{129}$Xe polarization was about 10%. A gas mixture of 10% $N_2$, 88% He, and 2% Xe (natural abundant $^{129}$Xe) was flowed through the hyperpolarizer, the resulting gas was guided to the NMR spectrometer and directly bubbled into the MOF dispersed solution at a flow rate of 0.1 L/min. The sample tube was maintained at a pressure of 53 PSI and a temperature of 298 K with the VT unit.

During the HP $^{129}$Xe CEST NMR experiments, the gas mixture was bubbled directly into the sample tube for 20 seconds. After a 3 seconds delay to allow the bubbles to collapse, continuous wave (CW) pulses were applied to selectively saturate the Xe@MOL peak (10 s with a 1~5 μT field). This was followed by the acquisition of a spectrum. Each spectrum was acquired in a single scan. NMR spectra for CEST were processed using 6 Hz line broadening filter. The gaseous $^{129}$Xe signal was defined as 0 ppm. Saturation contrast represents the normalized difference between on-resonance and off-resonance signals. CEST effect = (Off-Resonance - On-Resonance) / Off-Resonance.

*Bloch-McConnell equation*

The normalized CEST spectra were fitted according to the Bloch-McConnell (BM) equation.[2] Without loss of generality, it is assumed the saturation pulse is applied along the x-axis. In the rotating lab frame, we use superscripts $a$ and $b$ to show parameters of bulk pool (free $^{129}$Xe in solution) and dilute pool (captured $^{129}$Xe),[3] respectively. The BM equation in matrix form are the following:[4]

$$\frac{dM(t)}{dt} = A \cdot M \tag{S1}$$

Where

$$A = \begin{vmatrix} -R_2^a - k_{ab} & \Delta\omega & 0 & k_{ba} & 0 & 0 & 0 \\ -\Delta\omega_a & -R_2^a - k_{ba} & \omega_1 & 0 & k_{ba} & 0 & 0 \\ 0 & -\omega_1 & -R_1^a - k_{ba} & 0 & 0 & k_{ba} & R_1^a M_0^a \\ k_{ab} & 0 & 0 & -R_2^b - k_{ba} & \Delta\omega_b & 0 & 0 \\ 0 & k_{ab} & 0 & -\Delta\omega_b & -R_2^b - k_{ba} & \omega_1 & 0 \\ 0 & 0 & k_{ab} & 0 & -\omega_1 & -R_1^b - k_{ba} & R_1^b M_0^b \\ 0 & 0 & 0 & 0 & 0 & 0 & 0 \end{vmatrix} \quad \text{(S2)}$$

and

$$M(t) = \left| M_x^a(t) \quad M_y^a(t) \quad M_z^a(t) \quad M_x^b(t) \quad M_y^b(t) \quad M_z^b(t) \quad 1 \right|^T \quad \text{(S3)}$$

Where $M_0^a$ and $M_0^b$ denote the thermal equilibrium magnetizations of the free $^{129}$Xe and captured $^{129}$Xe, respectively. $f_B$ is given by $M_0^b / M_0^a$ which is defined as the ratio of capture $^{129}$Xe and free $^{129}$Xe. $R_1^a$, $R_2^a$, $R_1^b$, and $R_2^b$ represent the longitudinal and transverse relaxation rates of free $^{129}$Xe and captured $^{129}$Xe, respectively. $k_{ab}$ is the exchange rate from free $^{129}$Xe to captured $^{129}$Xe and vice versa, and $k_{ab} = f_B \cdot k_{ba}$. $\Delta\omega_a$ and $\Delta\omega_b$ are given by $\omega_a - \omega_{rf}$ and $\omega_b - \omega_{rf}$, where $\omega_a$ and $\omega_b$ are the Larmor frequencies of free $^{129}$Xe and captured $^{129}$Xe, respectively, and $\omega_{rf}$ is the frequency of the saturation pulse. $\omega_1$ is the amplitude of the saturation pulse. $M_x^a(t)$, $M_y^a(t)$, $M_z^a(t)$, $M_x^b(t)$, $M_y^b(t)$, $M_z^b(t)$ represent the magnetization of free $^{129}$Xe and captured $^{129}$Xe in x/y/z directions at time $t$.

The solution of the above BM equation can be given by

$$M(t) = e^{At_{sat}} \cdot M(0) \quad \text{(S4)}$$

$t_{sat}$ is the saturation time and $M(0)$ is the initial value of $M(t)$ $_{at}$ $t = 0$.

For the case of hyperpolarized nuclei

$$M(0) = |0 \quad 0 \quad P \cdot M_0^a \quad 0 \quad 0 \quad P \cdot M_0^b \quad 1|^T \quad \text{(S5)}$$

Where $P$ represents the signal enhancement factor of $^{129}$Xe via the optical pumping techniques. Due to the strong signal enhancement of hyperpolarization, the magnetization of hyperpolarized $^{129}$Xe is always much larger than the thermal equilibrium magnetization. For simplicity's sake, the value of $P$ is set to 10,000.

The simulated Hyper-CEST spectra are given by

$$Z(\omega_{rf}) = \frac{M_z^a(\omega_{rf})}{P \cdot M_0^a} \quad \text{(S6)}$$

After Xenon gas delivery to the sample, $^{129}$Xe CEST spectra were acquired with

different delay times ($T_d$) to estimate the $R_1^a$ value of free $^{129}$Xe in solution. For the case of hyperpolarized nuclei, the relationship between signal intensity and delay time can be given by

$$I(T_d) = I(0) \cdot e^{-R_1^a T_d} \quad \text{(S7)}$$

$I(T_d)$is the signal intensity with $T_d$ delay time, $I(0)$ is the signal intensity without delay time. The $R_1^a$ value was obtained by fitting the NMR signal intensity for different delay times to equation 1.[2]

The multiple Hyper-CEST spectra were fitted to the BM equation (Figure S7a); the parameters were varied in the fitting. The fitted parameter values of $R_2^b$ and $k_{ba}$ were listed in Table 1.

*HP $^{129}$Xe CEST MRI*

$^{129}$Xe MRI was generated with RARE sequence with eight-echo trains and 3 ms effective echo time. Including bubbling, wait and saturation times, the overall repetition time (TR) was 28 seconds. 10-second CW saturation pulses with a field strength of 2.5 to 10 μT were employed. All images were axial without slice selection, and the k-space matrix comprised 32 points in the readout dimension and 32 phase-encoding points. The field of view was 30 mm by 30 mm.

The MR images were processed using in-house written Matlab scripts (R2014a, MathWorks, Natick, MA). The 32×32 image matrix was interpolated into a 64×64 matrix and segmented using 0.2 times the maximum value of the off-resonance image as the threshold. The CEST effect of each pixel was then calculated using the formula CEST effect = (Off-Resonance - On-Resonance) / Off-Resonance, pixel by pixel.

*Establishment of the HP $^{129}$Xe CEST MRI based-3D map to quantify the MOL concentration*

After conducting MRI experiments to measure the chemical exchange saturation transfer (CEST) effects, we investigated the impact of different saturation field strengths and concentrations of MOL materials (Figure 1d). To analyze the data, we utilized MATLAB's Curve Fitting Toolbox and employed the cubic spline method to

create a distribution map of CEST effects in relation to saturation field strengths and MOL concentrations. Within the range of saturation field strengths and MOL concentrations employed in our experiments, the interpolated CEST distribution map was used to predict the corresponding CEST effect at a specified saturation field strength and concentration of MOL (Figure 1e). Thus, the content of MOL could be quantified by using the developed 3D-map.

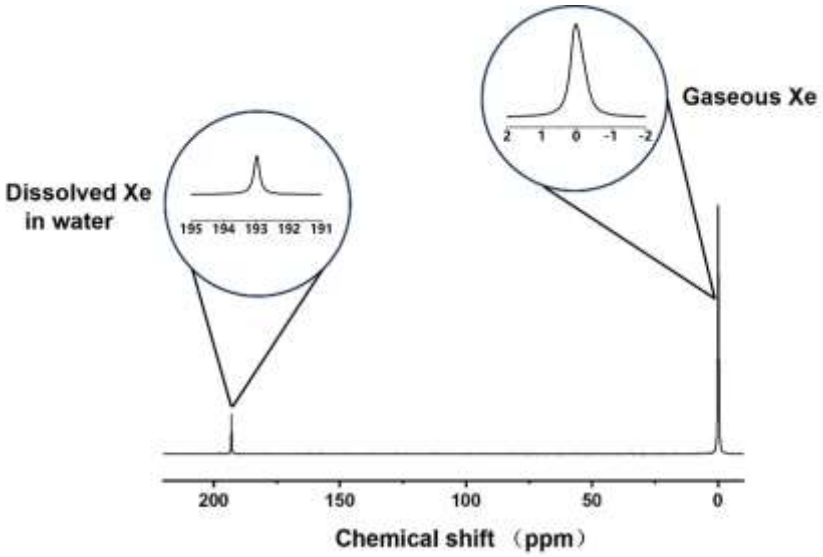


**Figure S6.** $^{129}$Xe NMR spectra of water dissolved with HP $^{129}$Xe.

Similar to the function of tetramethylsilane in $^{1}$H NMR, gaseous Xe was used as the standard, with a chemical shift of 0 ppm. The introduction of HP $^{129}$Xe gas into water produced a strong signal at 193 ppm (Figure S6), indicating the presence of dissolved free $^{129}$Xe.

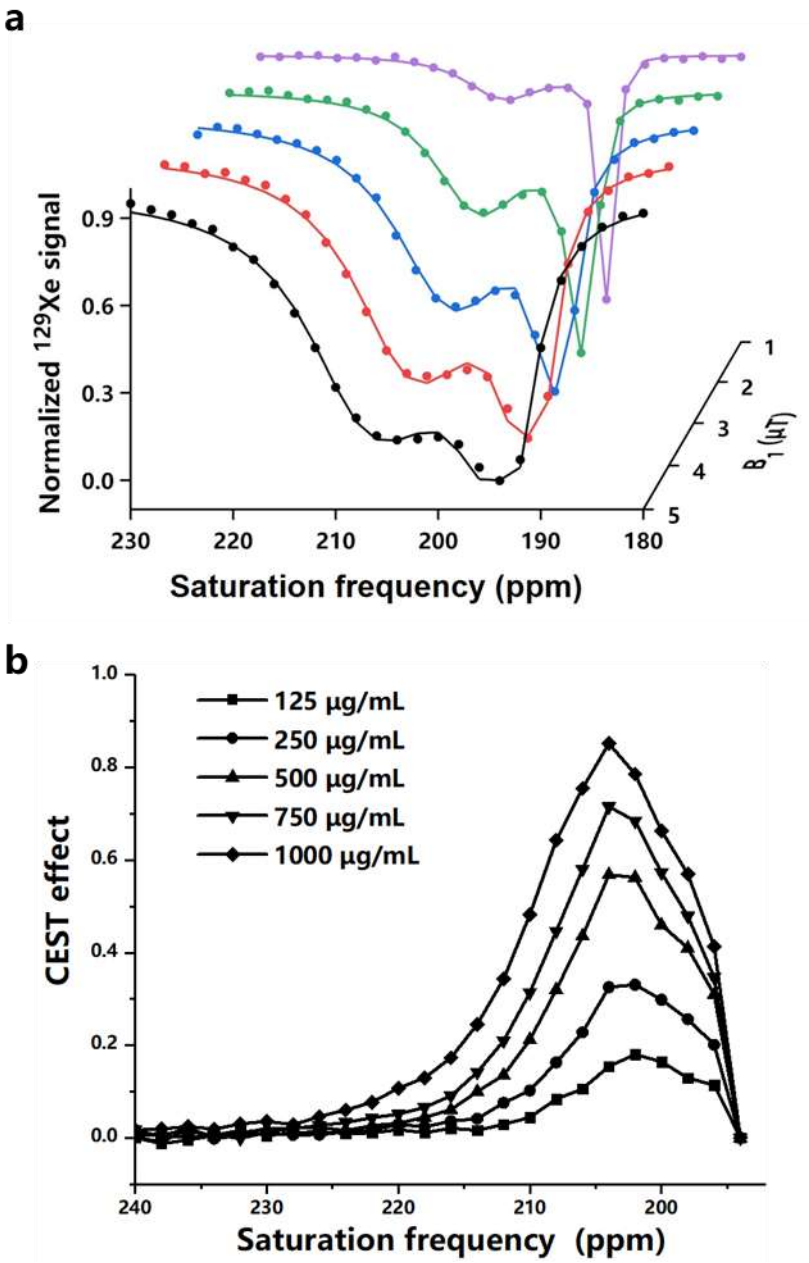


**Figure S7.** (a) The HP $^{129}$Xe CEST spectra of MOL fitted to the BM equation with RF irradiation under a $B_1$ field at 1, 2, 3, 4 and 5 μT. (b) The MTR spectra revealed the CEST effect exclusively from $^{129}$Xe in the MOL nano-hosts.

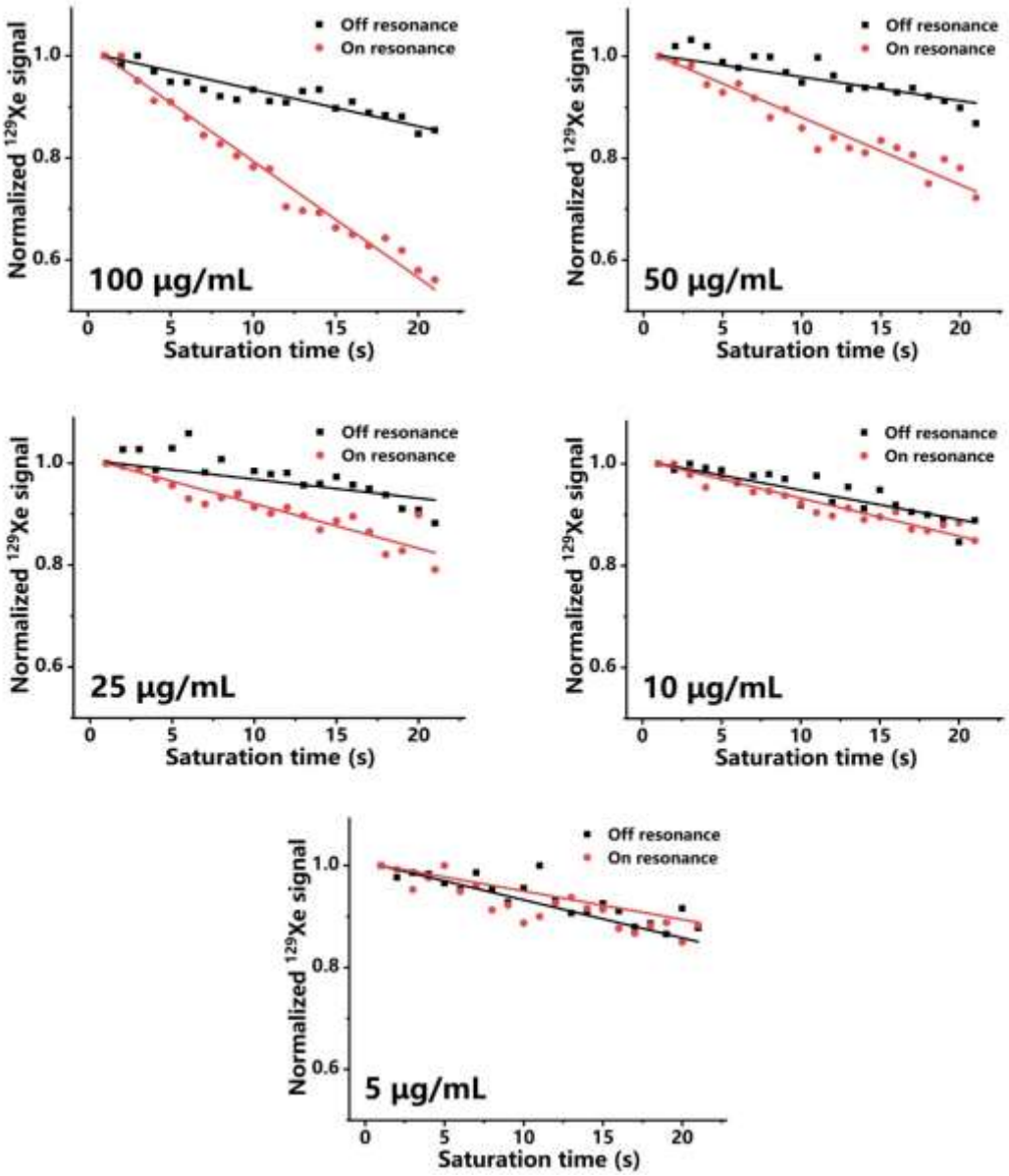


**Figure S8.** Detection limit of HP $^{129}$Xe CEST signal in MOL aqueous solution. Perform the same saturation time for different concentrations (100, 50, 25, 10 and 5 μg/mL) of MOL.

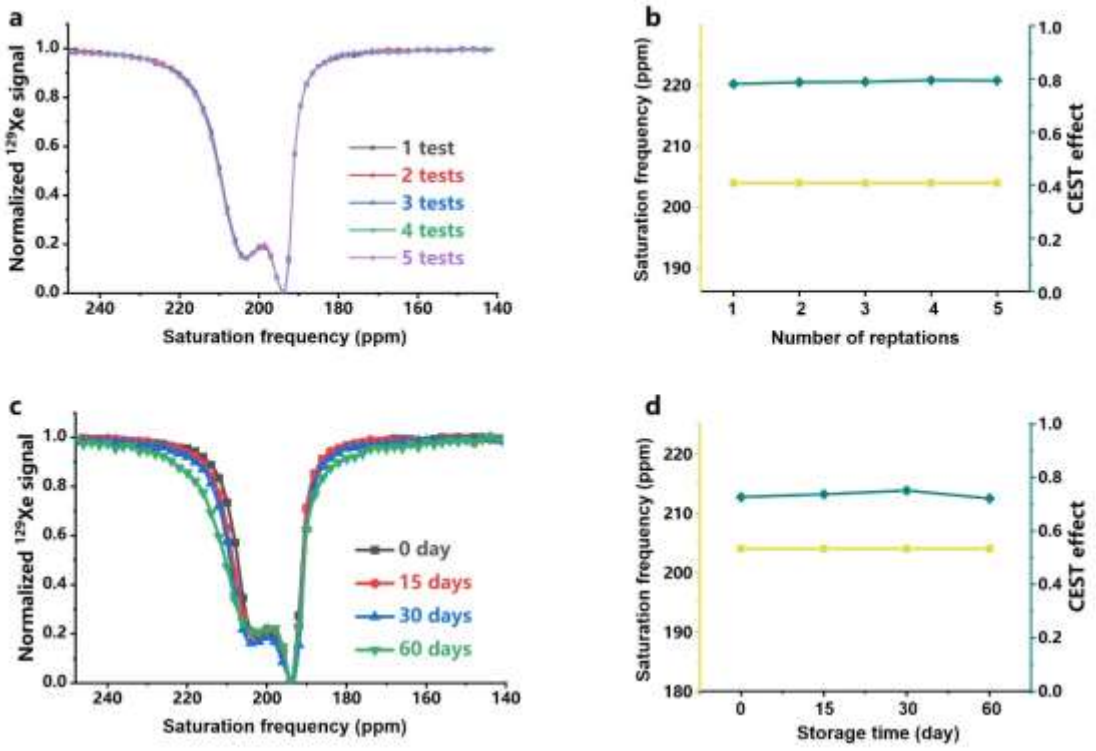


**Figure S9.** Signal stability of MOL nano-hosts. (a) HP $^{129}$Xe CEST spectra of MOL during 5 times of tests. (b) Saturation frequency and CEST effect analysis showed that the pore structure of MOL remains stable in aqueous solution after 5 times of tests. (c) The HP $^{129}$Xe CEST spectra of MOL at room temperature within 60 days. (d) Saturation frequency and CEST effect analysis showed that the pore structure of MOL remains stable in aqueous solution for 60 days storage.

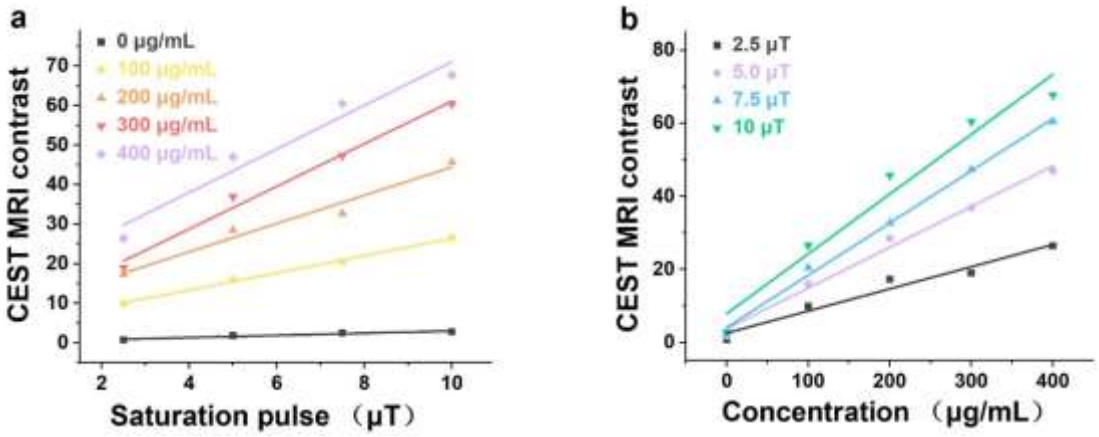


**Figure S10.** (a) The liner relationship between HP $^{129}$Xe CEST MRI contrast and saturation pulse (related parameters are shown in Table S1). (b) The liner relationship between HP $^{129}$Xe CEST MRI contrast and MOL concentration (related parameters are shown in Table S2).

**Table S1**. The fitting parameters that describe the liner relationship between HP $^{129}$Xe CEST MRI contrast and saturation pulse.

| Saturation pulse | Intercept | Slope | $R^2$ |
|---|---|---|---|
| 2.5 μT | 2.56 ± 1.74 | 0.06 ± 0.01 | 0.9799 |
| 5.0 μT | 3.78 ± 1.60 | 0.11 ± 0.01 | 0.9948 |
| 7.5 μT | 4.14 ± 1.24 | 0.14 ± 0.01 | 0.9962 |
| 10 μT | 7.88 ± 4.48 | 0.16 ± 0.01 | 0.9818 |

**Table S2**. The fitting parameters that describe the liner relationship between HP $^{129}$Xe CEST MRI contrast and MOL concentration.

| MOL concentration | Intercept | Slope | $R^2$ |
|---|---|---|---|
| 0 | 0.20 ± 0.34 | 0.28 ± 0.05 | 0.9688 |
| 100 μg/mL | 4.65 ± 0.60 | 2.17 ± 0.09 | 0.9967 |
| 200 μg/mL | 8.70 ± 3.15 | 3.58 ± 0.46 | 0.9838 |
| 300 μg/mL | 2.25 ± 2.86 | 5.38 ± 0.42 | 0.9940 |
| 400 μg/mL | 16.05 ± 5.80 | 5.50 ± 0.85 | 0.9770 |

**Table S3**. Quantification of the content of MOL in A549 cells using the $^{129}$Xe CEST MRI based 3D-map. The cells were collected after the MRI tests and analyzed with ICP-MS to further confirm the MOL content.

| **Sample** | **$^{129}$Xe CEST MRI contrast (%)** | **MOL uptake by cells (pg/cell)** | |
|---|---|---|---|
| | | Quantified by $^{129}$Xe CEST MRI | Measured by ICP-MS |
| **1** | 24.6 | 9.21 | 11.16 |
| **2** | 37.2 | 18.87 | 19.51 |
| **3** | 39.2 | 19.39 | 19.76 |
| **4** | 47.7 | 25.91 | 27.00 |
| **5** | 51.2 | 28.96 | 29.45 |

## *Section S3* Loading of ICG to MOL Nano-hosts

HP $^{129}$Xe MR techniques have been proven to be effective in detecting the microenvironment of cage-like hosts.[5] We hypothesized that this strategy could be applied to assess alterations in the microenvironment of nano-hosts following the introduction of drug molecules. In this study, we fabricated nanocarriers composed of a two-dimensional metal-organic framework, known as a MOL. The choice of MOL was based on its expansive surface area and uniform pore structure; thus, it was suitable for hosting drug molecules and generating a distinct $^{129}$Xe MR signal.

The obtained MOL was dispersed in DMF at a concentration of 1 mg/mL. Then, ICG and MOL were mixed in a DMF solution through sonication. The mixture was heated and stirred at 60℃ for 12 h in the dark. After cooling to room temperature, the mixture was centrifuged at 13,000 rpm for 30 min to remove free drug molecules in solution. The solids obtained at the bottom were re-dispersed in distilled water, sonicated for 3 min, and then centrifuged to remove residual DMF. For further purification, the ICG@MOL complex was dialyzed against Milli-Q water using a 3.5 kDa molecular weight cutoff dialysis membrane for 2 days. The concentration of the resulting ICG@MOL complex solution was carried out through ultrafiltration using an ultra-centrifugal filter (Millipore, 10K) at a speed of 4000 rpm for 30 min. The resulting ICG@MOL aqueous solution was stored in the dark at 4 °C.

The MOL water dispersion appears as a white and turbid mixture. Upon loading with ICG molecules, the mixture turns green, and the color deepens in proportion to the loading efficiency (Figure S11a). After centrifugation, a white or green solid is observed in the lower layer (Figure S11b), while the upper layer is clear and transparent, indicating successful loading of water-soluble ICG onto MOL. The loading efficiency is further confirmed by UV-vis spectra, thermogravimetric analysis (Figure S12), and $N_2$ sorption isotherms (Figure S13).

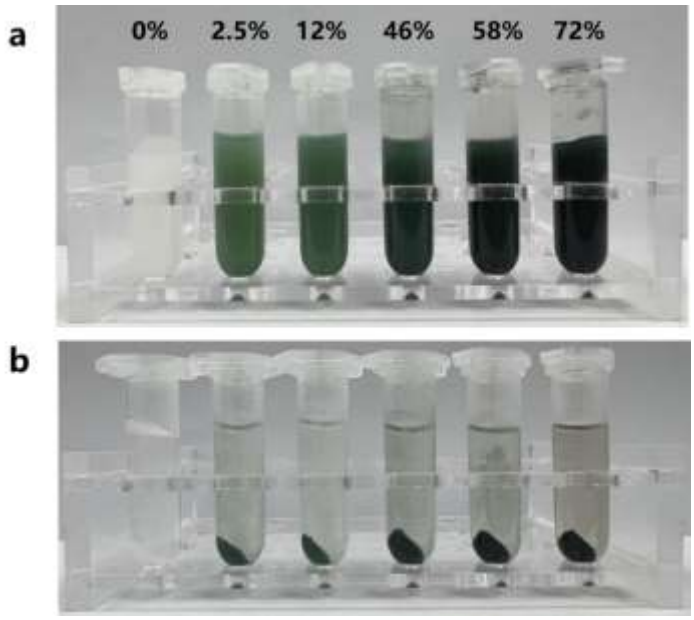


**Figure S11.** Photographs of ICG@MOL at loading efficiency levels of 2.5%, 12%, 46%, 58%, and 72%. Panel (a) displays ICG@MOL dispersed in water, while panel (b) shows ICG@MOL water dispersions after centrifugation at 13,000 rpm/min for 30 min.

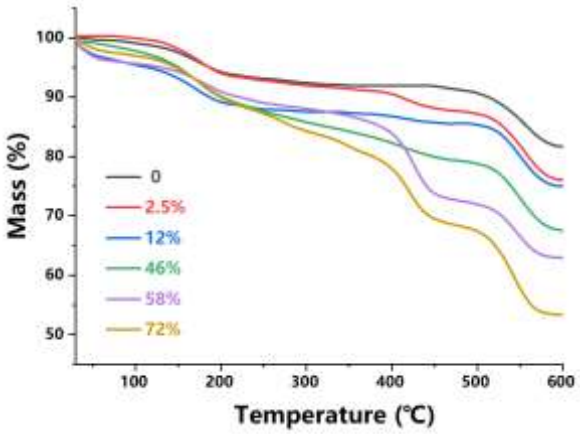


**Figure S12.** The thermogravimetric analysis of ICG@MOL at varying loading efficiencies of 2.5%, 12%, 46%, 58% and 72%.

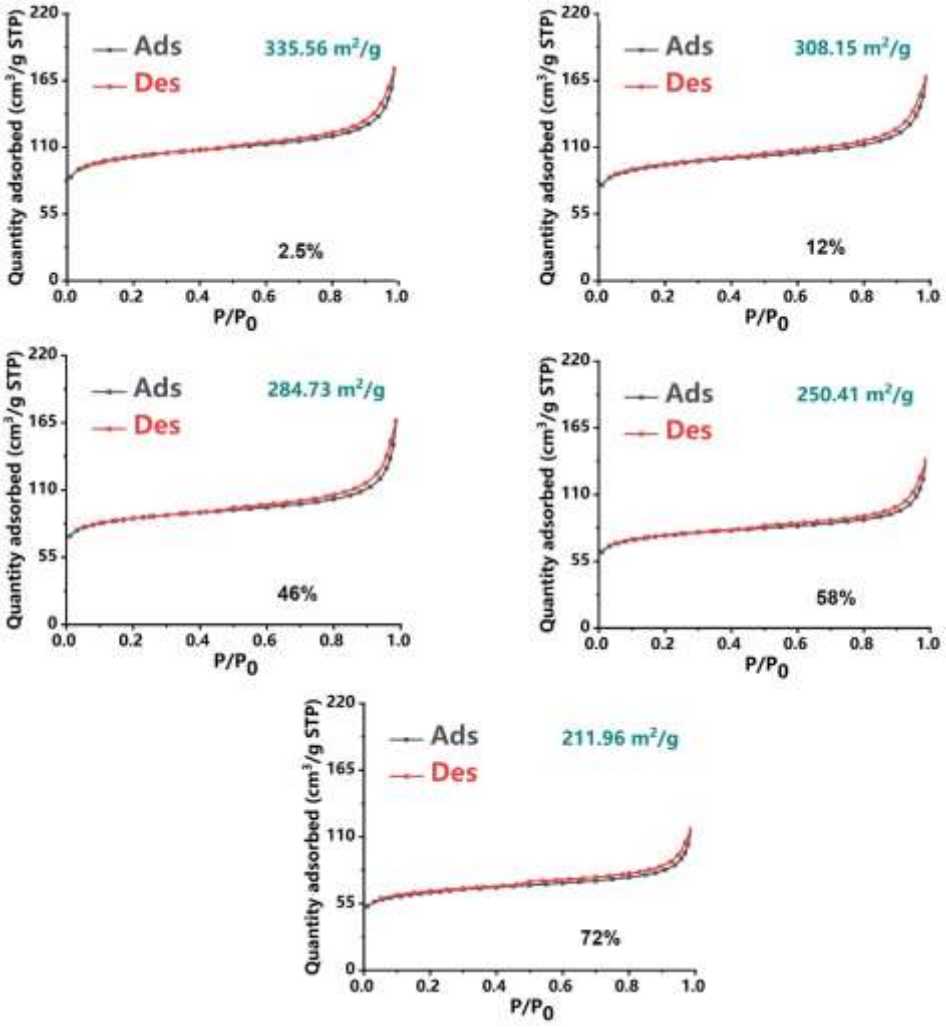


**Figure S13.** $N_2$ sorption isotherms of ICG@MOL at 77 K with different loading efficiency of 2.5%, 12%, 46%, 58% and 72%.

## *Section S4* Uptake of ICG@MOL by A549 Lung Cancer Cells

*Cell Culture*

A549 lung cancer cells were cultured in complete F12K medium, supplemented with 10% fetal bovine serum and 1% antibiotics (100 μg/mL penicillin and 100 μg/mL streptomycin), at a temperature of 37 °C in a humidified environment with 5% $CO_2$.

*Cellular uptake of ICG/MOL*

For magnetic resonance analysis, A549 cells were incubated with solutions of ICG, MOL, and ICG/MOL for 3 h, respectively. After removing the medium, the cells were carefully washed with sterile PBS 2~3 times. Then, cells were carefully separated from the culture flask by using a cell scraper. The obtained cells were dispersed in fresh F12K culture medium (containing 10% FBS, 1% penicillin-streptomycin) using a pipette, ensuring a smooth and repeated process to avoid generating gas bubbles. The cell dispersion solution was centrifuged at 300 XG for 3 min. After removing the supernatant, the cells were dispersed in PBS at a concentration of 1~2 $\times 10^7$ cells/mL. Finally, 2 mL of the cell dispersion was transferred to an NMR tube for magnetic resonance analysis.

After CEST MRI testing, the cells were collected and performed with ICP-MS to for further quantitative analysis of MOL content. The basic building block of MOL is describe as $Hf_6O_4(OH)_4(HCO_2)_6(carboxylate)_6$, with a molecular weight of 1743.18 and a measured metal content of 64 wt%.

For fluorescent imaging analysis, A549 cells were incubated with an ICG/MOL solution for 3 h. Then, the cells were washed three times with PBS 7.4 to remove any excess solution. To fix the cells, they were immersed in a 4% paraformaldehyde solution in PBS for 10 min at room temperature. After fixation, the cells were again washed with PBS and stained with DAPI for 5 min. Finally, the slides were washed three times with distilled water and examined under a Nikon A1 laser scanning confocal microscope. ICG@MOL was delivered to the A549 cells through coincubation. Confocal laser scanning microscopy (CLSM) showed that the fluorescence emitted by

ICG accumulated around the cell nucleus (Figure S15), demonstrating the successful uptake of ICG@MOL by A549 cells.

*Cytotoxicity Assay*

To assess the cytotoxicity of MOL, a Cell Counting Kit-8 (CCK-8) assay was performed. A549 cells were seeded at a density of $1 \times 10^3$ per well in a 96-well plate, with each well containing 100 μL of media. After 24 h, the cells were treated with different concentrations (0, 25, 50, 100, and 200 μg/mL) of MOL and ICG@MOL. Following incubation, 10 μL of CCK-8 reagent was added to each well, and the cells were further incubated for 2 h. Cells treated with normal medium served as controls, and the absorbance values were measured using a microplate reader.

*3D Cell Culture*

A549 cells were plated in U-bottom ultralow attachment 96-well plates at a density of $1 \times 10^5$ per well and incubated for 3 days in 200 μL of F12K medium supplemented with 10% FBS. Subsequently, the medium was replaced with 100 μL of F12K solution containing different forms of nanoparticles and incubated for the appropriate time. In the case of ICG@MOL, the incubation time was 3 h. After removing the supernatant, the 3D cell cultures were gently washed with PBS and transferred to a 35 mm glass bottom cell culture dish. Images were captured using a confocal laser scanning microscope with XYZ imaging (excitation wavelength: 640 nm; Z-axis step size: 10 μm). The 3D cell culture studies (Figure S16a, Figure S16b) further confirmed that the fluorescent signal from ICG@MOL could be observed at different Z-axis positions. Analysis of the relative fluorescence intensity (Figure S16c) indicated that the majority of the delivered ICG@MOL was located in the middle layer of the tumor cell spheres, confirming its effective penetrability. After analyzing the ICG@MOL-treated A549 cells, the MOL content remained stable even after 6 h of treatment (Figure S16d).

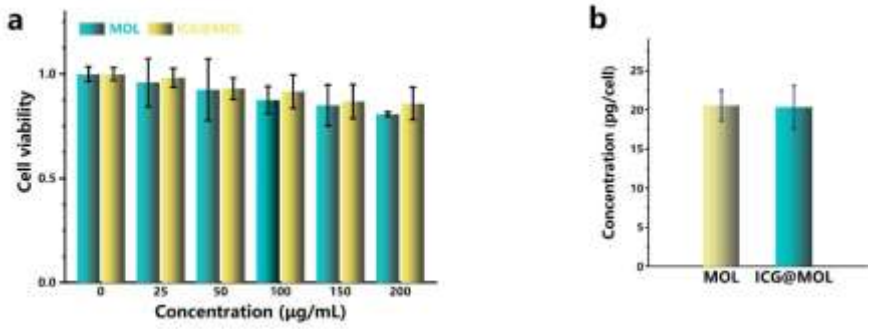


**Figure S14.** Evaluation of the biosafety and content of MOL in A549 cells. (a) Viability of A549 cells treated with various concentrations of MOL and ICG@MOL using the CCK-8 test. (b) Determination of the amount of MOL retained in A549 cells after 4 h of incubation with ICG or ICG@MOL (incubation concentration: 100 μg/mL for MOL).

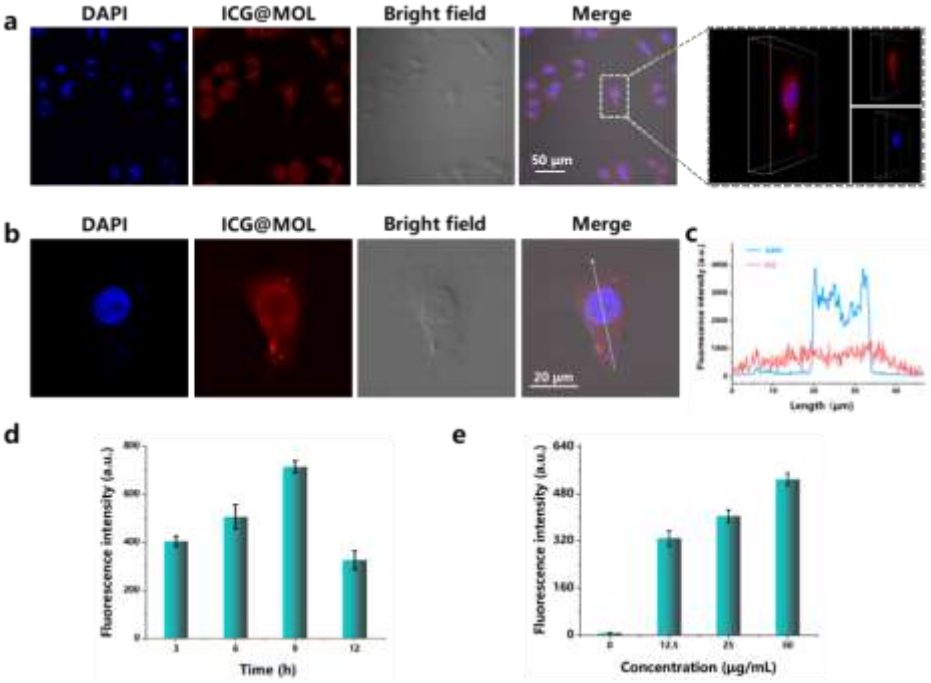


**Figure S15**. Delivery of ICG@MOL to the lung cancer A549 cells. (a) CLSM images of the A549 cells treated with 20 μg/mL of ICG@MOL for 3 h. The blue fluorescence represented the dsDNA in the nucleus that binds to 4',6-diamidino-2-phenylindole (DAPI), the red fluorescence originated from the loaded ICG. (b) Distribution of ICG/MOL in A549 cells and (c) quantitative analysis indicating the presence of ICG molecules in the cytoplasm and nucleus of A549 cells. (d) Fluorescence changes of ICG@MOL in A549 cells with varying incubation times and (e) incubation concentrations.

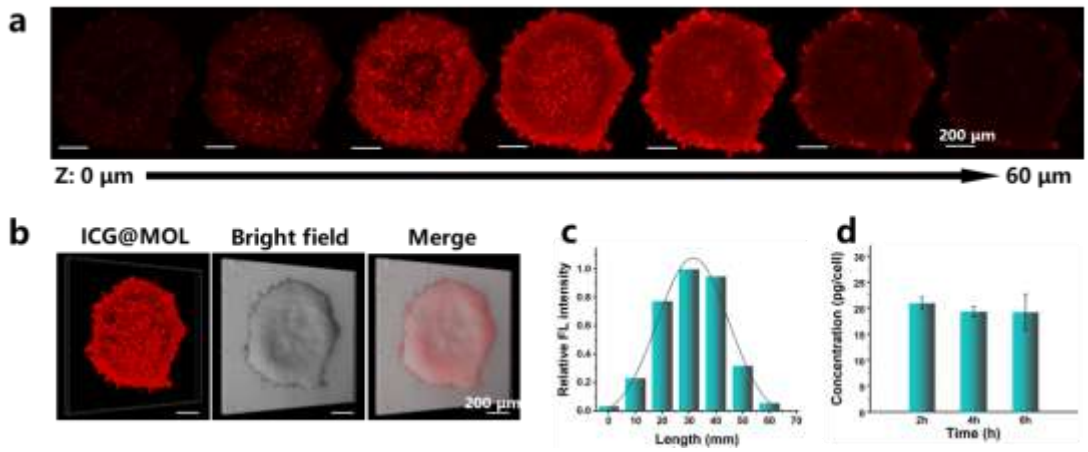


**Figure S16**. CLSM images of a A549 3D cell sphere (a) in different layers, (b) reconstructed 3D image indicating the penetration of ICG@MOL. (c) Quantitative analysis of the fluorescence intensity of ICG@MOL in the A549 3D cell spheroids at different layers. (d) Amount of MOL retained in the A549 cells at different times after completion of the incubation with ICG@MOL.

## *Section S5* Accumulation of ICG@MOL by Tumors

*Animals and Tumor Model*

Male Balb/c nude mice (4~5 weeks old, weighing 18~20 g, male) were procured from Beijing Vital River Laboratory Animal Technology Co., Ltd. All experimental procedures were conducted with the approval of the Animal Care and Use Committees at the Innovation Academy for Precision Measurement Science and Technology, Chinese Academy of Sciences. To establish A549 tumor xenograft models, the mice were subcutaneously inoculated with 200 μL of A549 cells in PBS with a concentration of $1\times10^8$ cells/mL on their right hind leg.

*In Vivo Homologous Targeting of ICG@MOL revealed by fluorescent imaging and photoacoustic imaging*

After the tumor had grown to the desired size, 10 mice were divided equally into two groups. Both groups were intravenously injected with 200 μL of ICG and ICG@MOL, respectively, at the same concentration as the ICG group. Prior to injection and at 3, 6, 12, 24, 48, and 72 h post-injection, the mice were subjected to fluorescence imaging using an IVIS Spectrum imaging system ($E_x$: 745 nm; $E_m$: 840 nm). Within 3 h of intravenous injection, the fluorescence signals (Figure S17a) primarily localized in the abdominal region and at the tumor sites. The ICG@MOL signal decayed more slowly when compared to the ICG control and was significantly enriched in the tumor, perhaps due to the enhanced penetration and retention (EPR) effect of the nanoparticles. The strong fluorescence intensity of ICG@MOL remained stable in the tumor for 72 h, indicating successful enrichment and prolonged presence within the tumor.

Photoacoustic imaging (PAI) was performed on A549 tumor-bearing mice to assess the efficacy of ICG and ICG@MOL nanoparticles. Following tail vein injection, enhanced photoacoustic signals were observed, specifically delineating the tumor in the ICG@MOL group (Figure S18a). The robust photoacoustic signal at the tumor periphery confirmed that ICG@MOL nanoparticles accumulated at the tumor site and gradually diffused from the outer region to the inner area. The overall signal intensity

reached its peak 3 h post-injection, which was consistent with the results from fluorescence imaging.

Comparatively, the fluorescent and photoacoustic intensity of ICG@MOL within the tumor was 1.47 times and 1.67 times higher at 3 h, and 2.21 times and 1.46 times higher at 72 h, respectively, compared to the ICG group (Figure S17b, Figure S18b). This enhanced accumulation can be attributed to the enhanced permeability and retention (EPR) effect of ICG@MOL. To further investigate the biodistribution, mice were dissected at 72 h post-injection, and fluorescence imaging using the IVIS Spectrum was performed on major organs and tumors. The tumor sites of ICG@MOL-injected mice exhibited more intense fluorescence (Figure S19). Additionally, the fluorescence and photoacoustic signals from tumors displayed a similar pattern, suggesting high tumor accumulation of ICG@MOL after injection (Figure S20).

Further analysis of tumor sections confirmed the *in vivo* penetration ability of ICG@MOL in tumor tissues (Figure S22). ICG@MOL successfully reached the tumor tissue and had an extended residence time compared to ICG. Under the same ICG dosage, the fluorescence intensity from mice injected with ICG@MOL was 1.81 times higher than that of ICG-injected mice (Figure S22b). Isolated organs and tumors were then processed for ICP-MS to measure the absorbed $Hf^{4+}$ content (Figure S21). The results showed that ICG@MOL nanosheets primarily accumulated in the liver, lung, and tumor, consistent with the imaging results. These findings demonstrate the superior tumor accumulation and extended residence time of ICG@MOL following intravenous injection.

*In vivo Biosafety of ICG@MOL*

Mice were sacrificed 72 h post-injection of ICG@MOL. Tumors and major organs (heart, liver, spleen, lung, and kidney) were extracted and fixed using 4% paraformaldehyde for later paraffin embedding, followed by tissue section H&E staining. Serum and blood were obtained by excising the eyeballs from the mice for blood biochemistry indicators measurement of the liver and spleen, conducted by

Servicebio, Wuhan.

No detectable pathological changes in major organs were observed in ICG@MOL treated groups (Figure S23), indicating that the ICG@MOL had good biocompatibility. Blood routine examination and blood biochemistry assays also indicated that ICG@MOL had little effect on liver function, kidney function and other physiological indexes (Figure S24). The above results demonstrated the good biocompatibility of ICG@MOL.

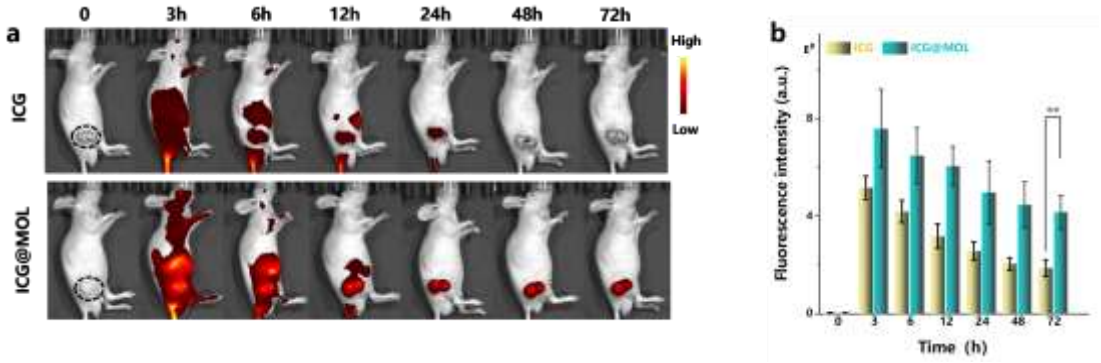


**Figure S17.** Demonstration of *in vivo* tumor targeting capability of ICG@MOL using fluorescence imaging. A549 tumor-bearing mice were intravenously injected with either ICG or ICG@MOL. Subsequently, *in vivo* fluorescence imaging (a) and quantitative fluorescence intensity measurements (b) were performed over a 72-hour period. The tumor area was delineated by a black dashed line. All data represent the mean ± standard deviation (n = 3, *p < 0.05, **p < 0.01, and ***p < 0.001)

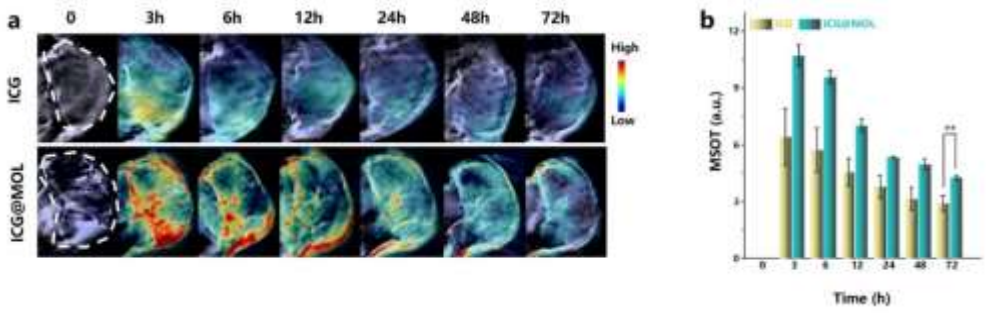


**Figure S18.** Demonstration of *in vivo* tumor targeting capability of ICG@MOL using photoacoustic imaging. A549 tumor-bearing mice were injected intravenously with

either ICG or ICG@MOL. Subsequently, *in vivo* photoacoustic imaging (a) and quantitative photoacoustic intensity measurements (b) were performed over a 72-hour period. The tumor area was delineated by a white dashed line. All data represent the mean ± standard deviation (n = 3, *p < 0.05, **p < 0.01, and ***p < 0.001)

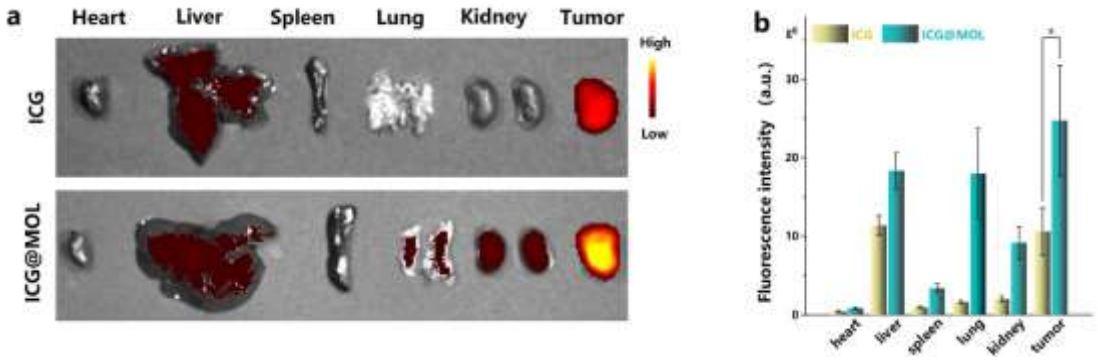


**Figure S19.** *Ex vivo* fluorescence images (a) and intensity measurements (b) of isolated organs. A549 tumor-bearing mice were intravenously injected with either ICG or ICG@MOL. Organs were collected 72 h after injection. All data represent the mean ± standard deviation (n = 3, *p < 0.05, **p < 0.01, and ***p < 0.001)

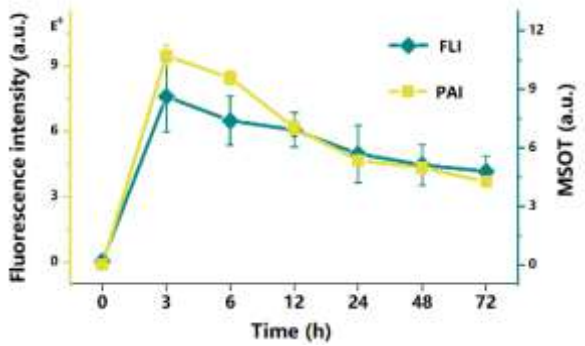


**Figure S20.** Temporal changes in fluorescence intensity (green) and photoacoustic intensity (yellow) of tumors (n=3) over time.

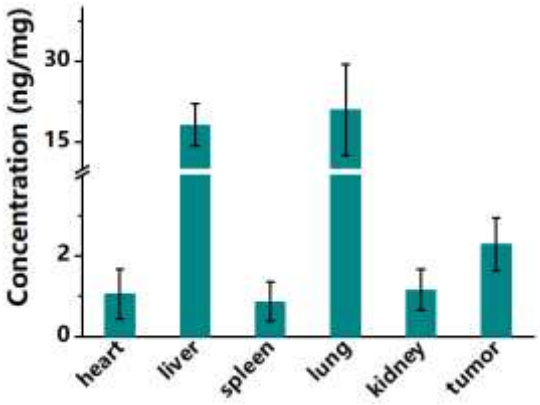


**Figure S21.** Measurement of MOL content in isolated organs and tumors at 72 h post injection of ICG@MOL using ICP-MS analysis.

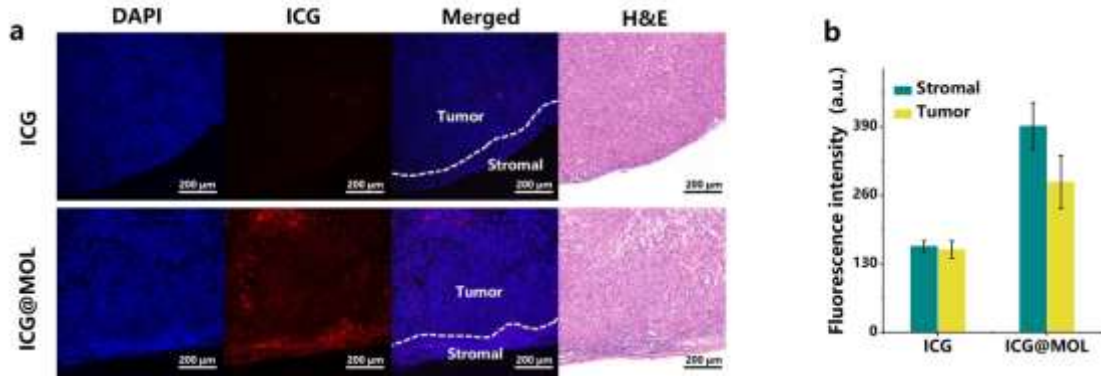


**Figure S22.** *Ex vivo* fluorescence images (a) of tumor tissues and fluorescence intensity measurements (b) of stromal and tumor regions.

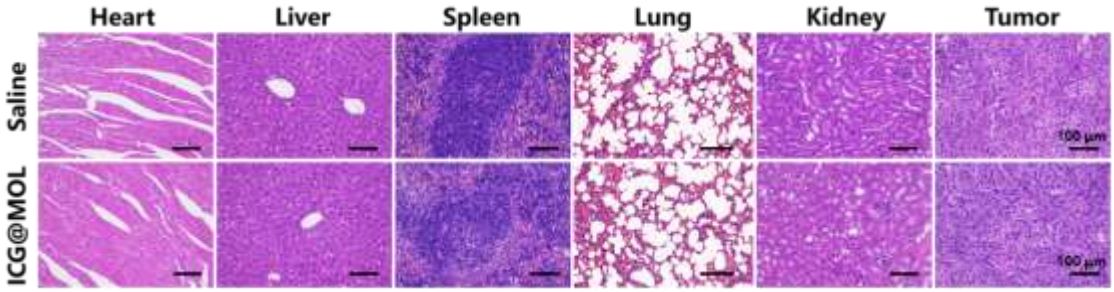


**Figure S23.** Hematoxylin and eosin (H&E) staining assay of major organs and tumor tissues after intravenous administration of saline and ICG@MOL.

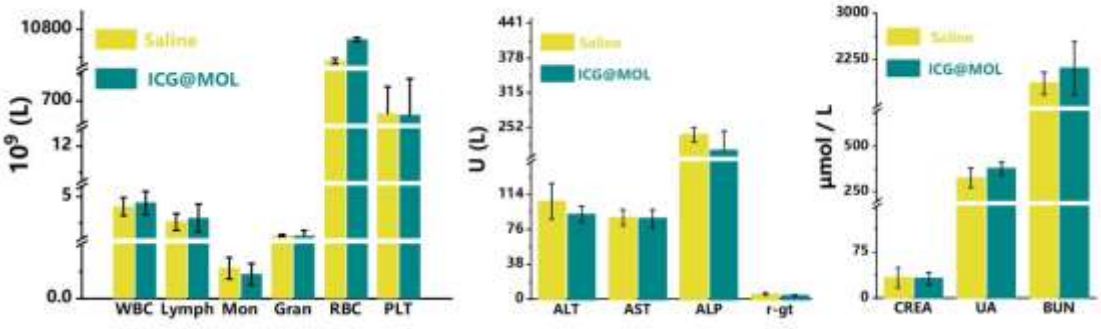


**Figure S24.** Evaluation of *in vivo* biocompatibility of ICG@MOL. (a) Concentration of main blood cells including white blood cells (WBC), lymphocytes (Lymph), monocytes (Mon), granulocytes (Gran), red blood cells (RBC), and platelets (PLT) after intravenous injection of saline and ICG@MOL. (b) Concentration of liver function-related enzymes including alanine aminotransferase (ALT), aspartate aminotransferase (AST), alkaline phosphatase (ALP), and gamma-glutamyltransferase (r-gt) after intravenous injection of saline and ICG@MOL. (c) Concentration of kidney function markers including creatinine (CREA), uric acid (UA), and blood urea nitrogen (BUN) after intravenous administration of saline and ICG@MOL.

***Section 6* Verify the Universality of the Developed HP $^{129}$Xe Sensing Approach**

To confirm the universality of our Xe sensing approach in detecting drugs in MOL, we further conducted experiments using the water-soluble anticancer drug doxorubicin hydrochloride (DOX) and the photosensitizer protoporphyrin IX (PPIX).

*Loading of DOX molecules to MOL nano-hosts*

First, we loaded DOX molecules to the MOL nano-hosts by dissolving DOX in distilled water at concentrations of 1, 2, 4, 10, 15, and 20 mg/mL, respectively. 1 mL of the prepared DOX solution was then added to 1 mL 2 mg/mL MOL water dispersion and stirred overnight at 25°C. Afterward, the mixture was centrifuged at 13,000 rpm for 30 min to remove any free DOX molecules in the solution. The resulting solids were re-dispersed in distilled water, sonicated for 1 minute, and centrifuged again to eliminate any residual DOX. To further purify the DOX@MOL complex, it was washed three times with distilled water. The concentration of the resulting DOX@MOL complex solution was determined through ultrafiltration using a Millipore ultra-centrifugal filter (10K) at a speed of 4000 rpm for 30 min. Finally, the DOX@MOL aqueous solution was stored in the dark at 4°C.

Doxorubicin appears as a bright red color when dissolved in water, while the MOL water dispersion appears as a white and turbid mixture. After loading DOX molecules into the MOL nano-hosts, the resulting mixture displayed a rose red turbid liquid (see Figure S25a). Upon centrifugation, the DOX remained a bright red solution, while the MOL settled as a white solid in the lower layer. The rose red DOX@MOL complex was successfully separated as a solid layer, and the upper layer solution appeared clear and transparent. The loading efficiency was further confirmed through UV-vis spectra.

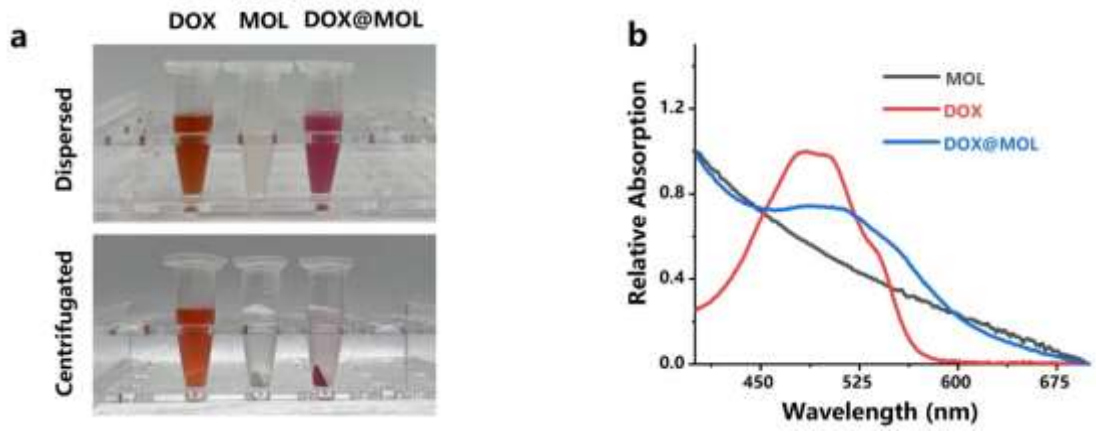


**Figure S25.** Loading DOX molecules into MOL nano-hosts. (a) Photographs of DOX, MOL and DOX@MOL when dispersed in water (up), water dispersions were centrifugated at 13000 rpm/min for 30 min (down). (b) UV-vis spectra of DOX, MOL and DOX@MOL.

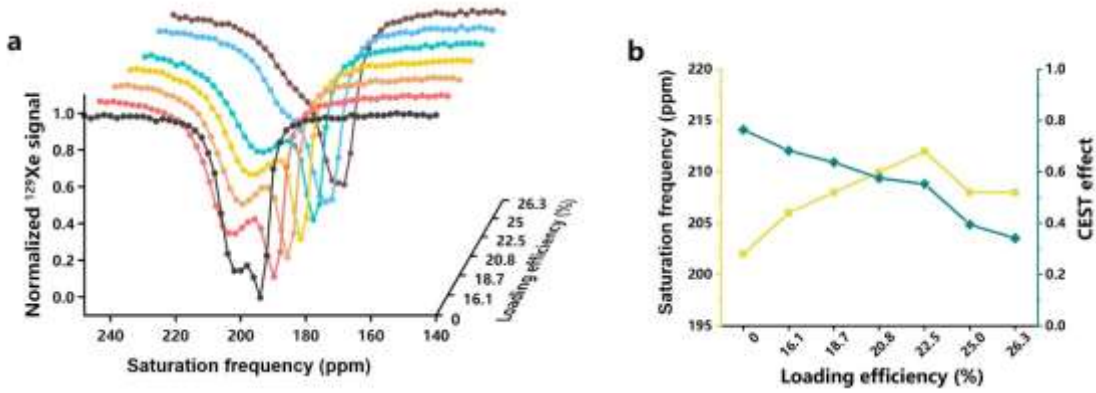


**Figure S26.** MR signal changes along with various loading efficiency. (a) HP $^{129}$Xe CEST spectra of DOX@MOL with various loading efficiency. (b) Saturation frequency and CEST effect of the nano-hosts continuously change with the increasing DOX loading efficiency.

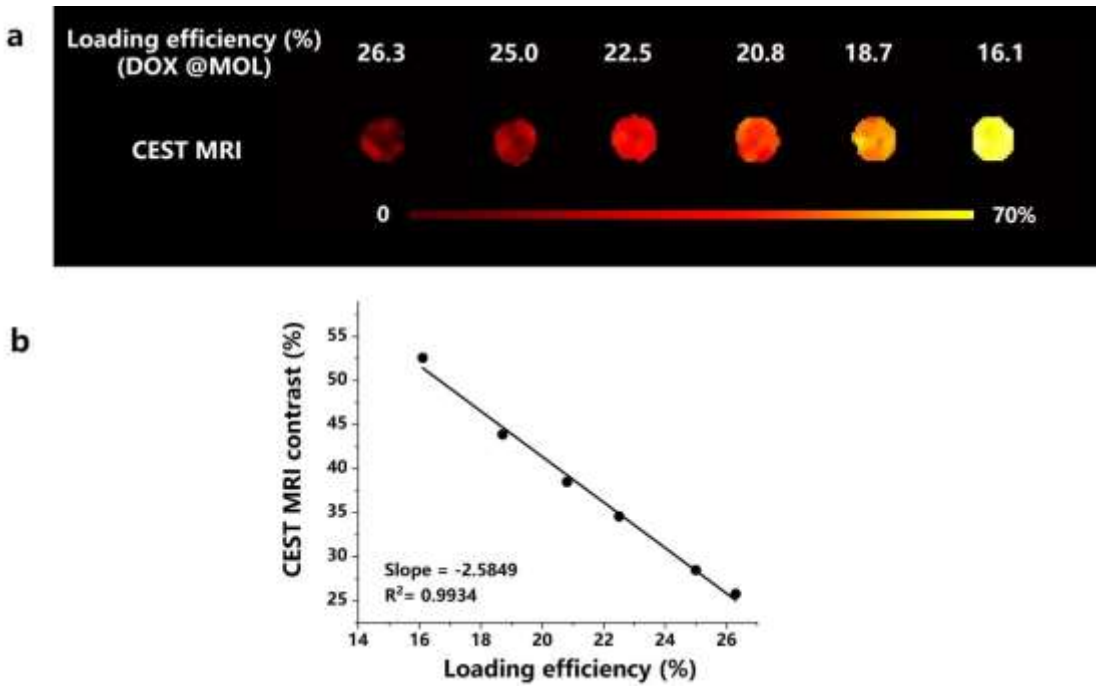


**Figure S27.** HP $^{129}$Xe MRI reveals the environment changes of MOL nano-hosts induced by the introduction of DOX molecules. (a) HP $^{129}$Xe CEST MRI of DOX@MOL with various loading efficiency. (b) HP $^{129}$Xe CEST MRI contrast is linear to the loading efficiency of DOX@MOL.

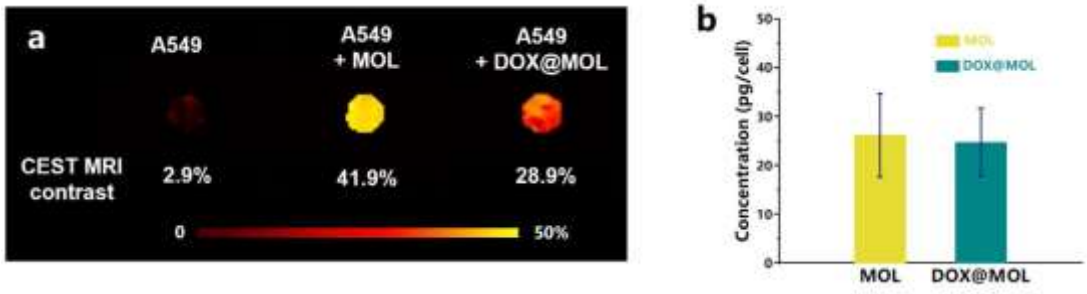


**Figure S28.** HP $^{129}$Xe CEST MR images of A549 cells treated with F12K medium, DOX@MOL and MOL. (b) Measurement of MOL content in single cell of A549 cells nitrolysis solution incubated with MOL and DOX@MOL after Hyper-CEST $^{129}$Xe MR images.

*Loading of PPIX molecules to MOL nano-hosts*

To load PPIX molecules into MOL nano-hosts, PPIX was dissolved in DMF at concentrations of 0.5, 1 and 2 mg/mL respectively.1mL of the resulting PPIX solution was then added to 1mL of 2 mg/mL MOL DMF dispersion and sonicated for 3 min to ensure uniform mixing. The mixture was heated and stirred at 60℃ for 12 h in the dark. After cooling to room temperature, the mixture was centrifuged at 13,000 rpm for 30 min to remove free PPIX molecules in solution. DMF

The solids obtained in the lower layer were re-dispersed in distilled water, sonicated for 3 min, and then centrifuged again to remove residual DMF. For further purification, the PPIX@MOL complex was dialyzed against Milli-Q water using a 3.5 kDa molecular weight cutoff dialysis membrane for 2 days. The concentration of the resulting PPIX@MOL complex solution was determined through ultrafiltration using an ultra-centrifugal filter (Millipore, 10K) at a speed of 4000 rpm for 30 min. The resulting PPIX@MOL aqueous solution was stored in the dark at 4 °C.

Prior to loading into MOL nano-hosts, PPIX appeared as a dark brown and turbid solution when dispersed in water. However, after loading, the mixture presented a brown and well-dispersed state (Figure S29a). During centrifugation, the majority of the dark brown solid settled in the lower layer, with some sticking to the wall of the centrifuge tube. The water dispersion of PPIX was significantly improved by loading into MOL nano-hosts. The brown PPIX@MOL complex was completely separated as a solid in the lower layer, while the upper layer solution appeared clear and transparent. The loading efficiency was further confirmed by UV-vis spectra.

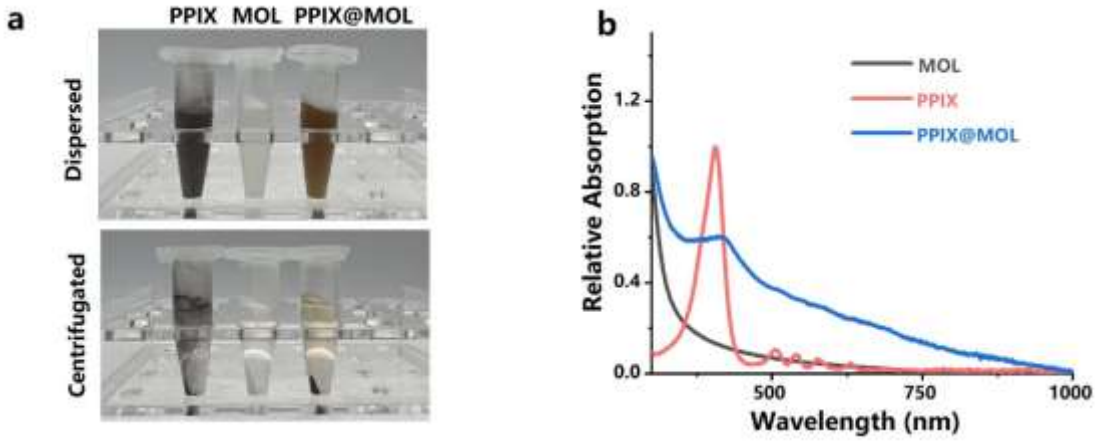


**Figure S29.** Loading PPIX to MOL. (a) Photographs of PPIX, MOL and PPIX @MOL when dispersed in water (up), water dispersions were centrifugated at 13000 rpm/min for 30 min (down). (b) UV-vis spectra of PPIX, MOL and PPIX@MOL.

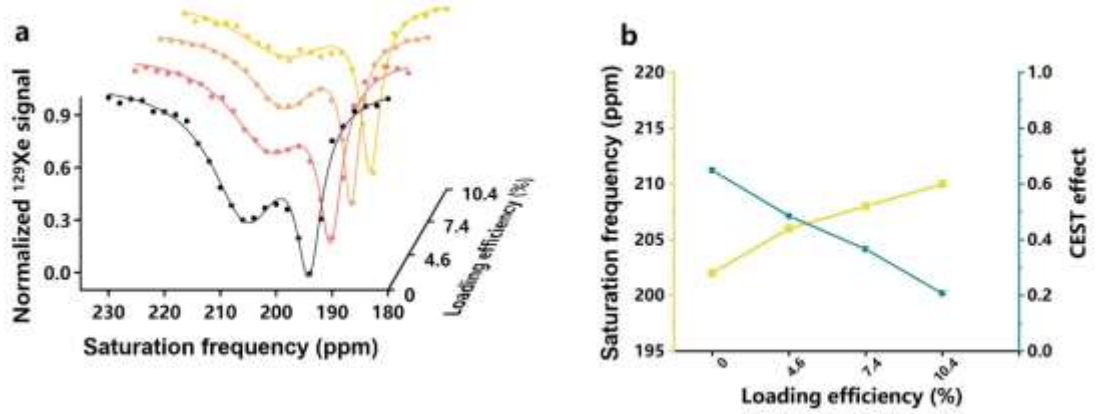


**Figure S30.** MR signal changes along with various loading efficiency. (a) HP $^{129}$Xe CEST spectra of PPIX@MOL with various loading efficiency. (b) Saturation frequency and CEST effect of the nano-hosts continuously change with the increasing PPIX loading efficiency.

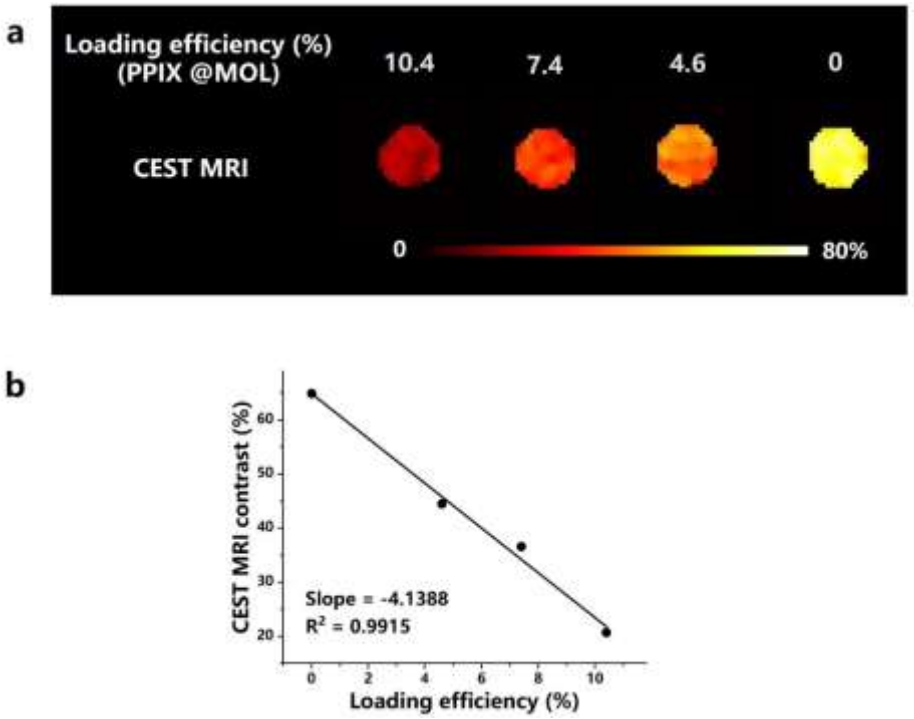


**Figure S31.** $^{129}$Xe MRI reveals the environment changes of MOL nano-hosts induced by the introduction of PPIX molecules. (a) $^{129}$Xe CEST MRI of PPIX@MOL with various loading efficiency. (b) $^{129}$Xe CEST MRI contrast is linear to the loading efficiency of PPIX@MOL.

**Supplementary references**


1. Cao, L.; Lin, Z.; Peng, F.; Wang, W.; Huang, R.; Wang, C.; Yan, J.; Liang, J.; Zhang, Z.; Zhang, T.; Long, L.; Sun, J.; Lin, W. Self-Supporting Metal-Organic Layers as Single-Site Solid Catalysts. *Angew. Chem., Int. Ed.* **2016**, 55, 4962-4966.
2. Kunth, M.; Witte, C.; Schroder, L. Quantitative chemical exchange saturation transfer with hyperpolarized nuclei (qHyper-CEST): sensing xenon-host exchange dynamics and binding affinities by NMR. *J. Chem. Phys.* **2014**, 141, 194202-194211.
3. Zaiss, M.; Bachert, P. Exchange-dependent relaxation in the rotating frame for slow and intermediate exchange-modeling off-resonant spin-lock and chemical exchange saturation transfer. *NMR Biomed.* **2013**, 26, 507-518.
4. Murase, K. Numerical Analysis of the Magnetization Behavior in Magnetic Resonance Imaging in the Presence of Multiple Chemical Exchange Pools. *Open J. Appl. Sci.* **2017**, 07, 1-14.
5. Angelovski, G.; Tickner, B. J.; Wang, G. Opportunities and challenges with hyperpolarized bioresponsive probes for functional imaging using magnetic resonance. *Nat. Chem.* **2023**, 15, 755-763.